

# Enhanced Lubricant Property of Flame-Sprayed Aluminum Coatings Additivated by Reduced Graphene Oxide Nanosheets

Yuting Xu<sup>1,2</sup> · Botao Zhang<sup>1</sup> · Songze Wu<sup>1</sup> · Yi Liu<sup>1</sup> · Xinkun Suo<sup>1</sup> · Hua Li<sup>1</sup>

Submitted: 8 April 2018 / in revised form: 27 September 2018 / Published online: 16 October 2018  
© ASM International 2018

**Abstract** Flame spraying was applied to prepare aluminum (Al)-reduced graphene oxide (rGO) composite coatings for the first time using ball-milled composite powders. The microstructure, tribological and electrochemical properties of the rGO-Al composite powders and coatings were investigated. Microstructural characterization for the composite powders reveals that rGO nanosheets adhered to Al particle surfaces after milling. Flattening and cold welding phenomena of Al particles were also recognized. The structure evolution of rGO as a function of the time of ball milling was also revealed. The results of coating microstructure investigation show that the rGO nanosheets were uniformly distributed in the coatings after coating deposition. The result of ball-on-disk testing shows that the addition of 0.3 wt.% rGO in the composite coatings brought about significantly enhanced lubricant performance. We believe that the results gained in this research would give insight into producing novel rGO-metal anti-friction materials.

**Keywords** ball milling · corrosion · flame spraying · rGO · wear

✉ Xinkun Suo  
suoxinkun@nimte.ac.cn

✉ Hua Li  
lihua@nimte.ac.cn

<sup>1</sup> Key Laboratory of Marine Materials and Related Technologies, Zhejiang Key Laboratory of Marine Materials and Protective Technologies, Ningbo Institute of Materials Technology and Engineering, Chinese Academy of Sciences, Ningbo 315201, China

<sup>2</sup> Nano Science and Technology Institute, University of Science and Technology of China, Suzhou 215123, China

## Introduction

As a two-dimensional (2D) carbonaceous material, graphene has been drawing great attention since it was first discovered in 2004 by Geim and coworkers (Ref 1). Graphene sheet is regarded as the thinnest material in the universe with a single layer of  $sp^2$  hybridized carbon atoms (Ref 2). This lattice can be wrapped up into 0D buckyballs, 1D nanotubes, or stacked into 3D graphite (Ref 3). Graphene sheets stacking together with multiple single layers have a thickness of around 0.335 nm and possess strong in-plane bonding but poor van der Waals interaction among the layers (Ref 3, 4). Due to the unique structural features, graphene has been reported to have remarkable properties, such as high thermal conductivity, superior mechanical properties and excellent electrical properties (Ref 5-9). The excellent properties make graphene the perfect potential reinforcement additive for many kinds of composites (Ref 10).

Up to now, several attempts have been made to fabricate polymer matrix composites reinforced with graphene. Mo et al. (Ref 11) added graphene into polyurethane as an excellent and promising building block material to improve the tribological property of the polymer. It was found that 0.25-0.5 wt.% addition of graphene sheets could bring about a remarkable enhancement of the tribological property. Chang et al. (Ref 12) also reported that well-dispersed 0.5-1.0 wt.% graphene sheets remarkably improved the wear resistance of the epoxy matrix. Moreover, graphene could also improve the corrosion resistance of UHMWPE in our previous investigation (Ref 13).

Similar to polymer/graphene composites, mechanical properties of metallic matrix can also be improved using graphene. Compared to pure aluminum coatings, Al/graphene composite coatings exhibited a 3.8-fold increase in

hardness and an 11-fold decrease in friction coefficient (Ref 14). Due to grain refinement, the peak hardness on the surface of graphene-reinforced Al6061 alloys increased to 1.3 GPa, while the peak hardness of Al6061 alloys was 0.5 GPa. Accordingly, the wear volume of the graphene-reinforced Al6061 alloys was reduced by 82% due to the self-lubricating nature of carbonaceous materials (Ref 15).

Many approaches have been attempted to fabricate metal/graphene composites, such as electrodeposition (Ref 16, 17), CVD (Ref 18, 19), friction stir process (Ref 15) and hot extrusion (Ref 6, 20). Thermal spraying, as one of the most widely used surface coating techniques and additive manufacturing processes, has a number of advantages including wide material applicability, cost efficiency, and easy on-site operation (Ref 21). However, metal/graphene composite fabrication using thermal spraying can hardly be found. Therefore, in this study, ball milling was applied for preparing rGO-Al composite powders. rGO nanosheets were incorporated into Al coatings using flame spraying. The functions of rGO on the electrochemical and tribological properties of Al coatings were characterized and elucidated.

## Materials and Experiments

### Preparation of rGO-Al Composite Powders

Graphite oxide was synthesized according to a modified Hummer's method (Ref 22, 23). Then, the graphite oxide was reduced by thermal reduction at 200 °C for 30 min in a vacuum furnace (0.1 Pa) following an established protocol (Ref 24). The Al powders with an average particle size of 54.0 μm (Changsha Tianjiu Metal Materials Co., Ltd, China) were used for preparing rGO-Al composite powders. The contents of rGO were 0.1, 0.3, and 0.5 wt.%, respectively. Morphology and particle size range of the Al powders are shown in Fig. 1. A planetary ball mill (QM-3SP4, Nanjing Nan Da instrument Co., Ltd, China) was employed to make rGO-Al composite powders. Stainless steel balls and vials were used, and the ball-to-powder weight ratio was 15:1. The rotation speed was set at 200 rpm, and argon gas was used to prevent oxidation of Al during milling. The ball milling duration was set at 2, 4, and 8 h, respectively.

### Fabrication of rGO-Al Composite Coatings

rGO-Al powders were deposited on mild steel plates (Q235B, 20 × 20 × 2 mm) using flame spraying (CDS 8000, Castolin, UK). Prior to spraying, the substrates were ultrasonically cleaned by acetone and then followed by air-drying and sand blasting using alumina. Acetylene was

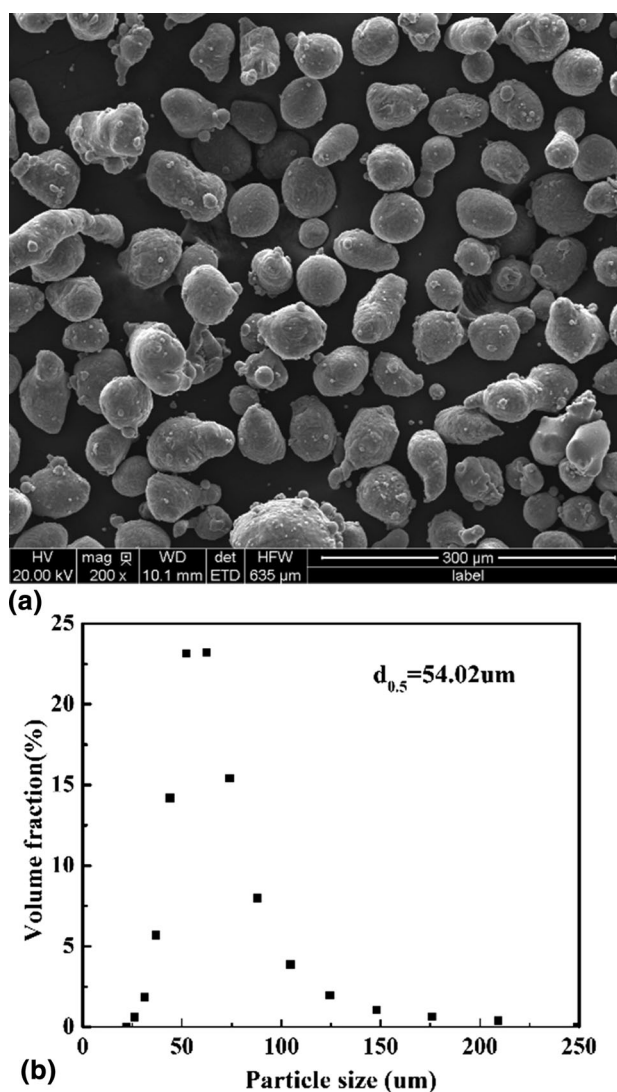


**Fig. 1** Surface morphologies (a) and size distribution (b) of the Al feedstock powder

employed as the fuel gas, and the pressure of oxygen and acetylene was fixed at 0.3 and 0.1 MPa, respectively. The flow rates of oxygen and acetylene were set at 0.25 and 0.30 m<sup>3</sup>/h, respectively. The feeding rate of powders was set at 15 g/min, and the spraying standoff distance was 250 mm from the nozzle exit to the sample surface.

### Microstructure Characterization

The morphologies of the powders and the coatings were examined using a field emission scanning electron microscope (FESEM, Quanta FEG 250, USA) equipped with an energy-dispersive spectrometer (EDS). Size distribution of the composite powders was analyzed by a particle size analyzer (Microtrac, S3500-special, USA). Raman microspectrometer (Renishaw inVia Reflex, Renishaw,

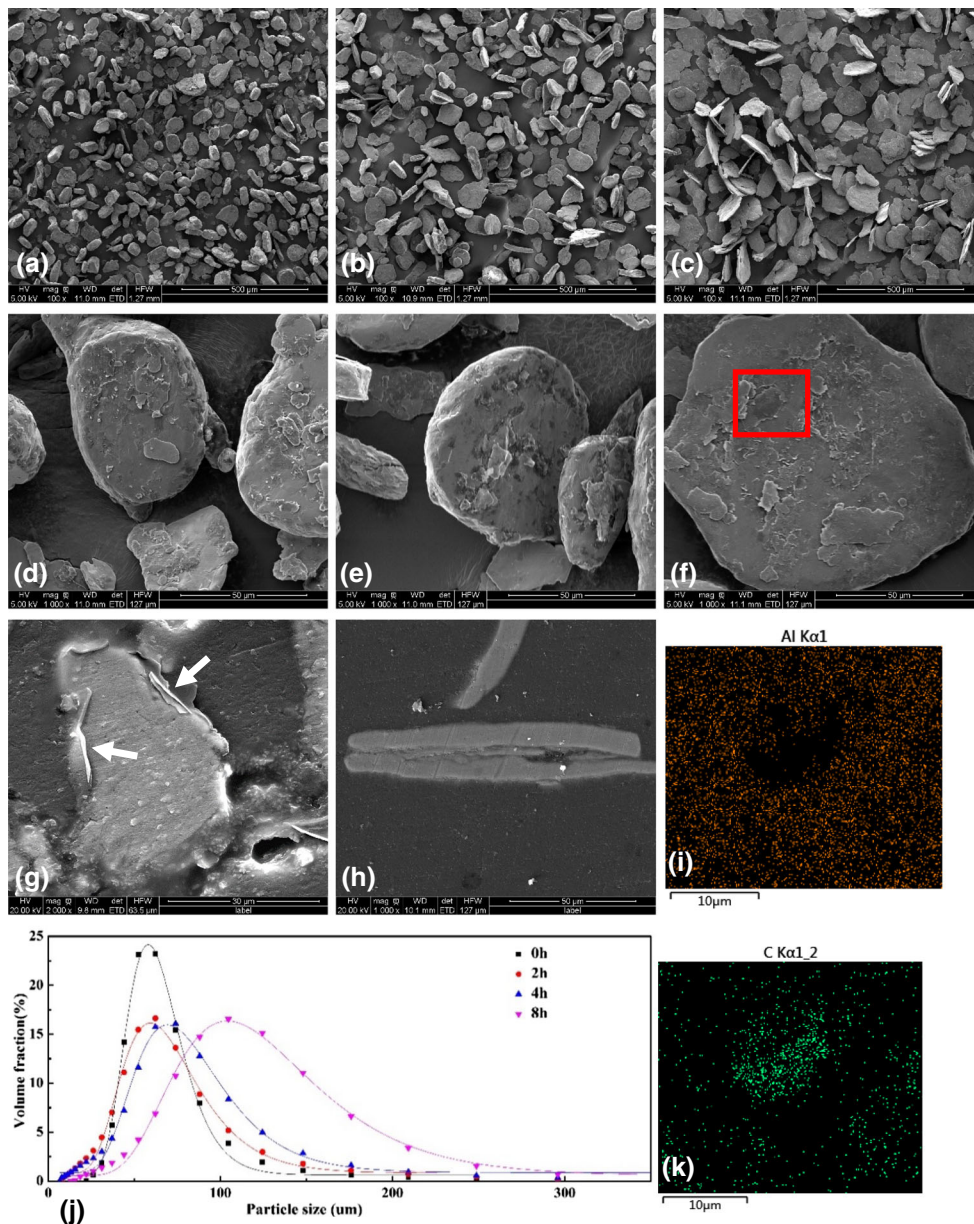


**Fig. 2** Surface morphologies and size distribution of the Al-0.1 wt.% rGO powder milled for 2 h (a, d), 4 h (b, e) and 8 h (c, f). Cross-sectional microstructures of the powder milled for 8 h (g, h), EDS

mapping analysis for rectangles in (f) (i, k), and particle size distribution of the composite powder (j)

Britain) with a laser wavelength of 532 nm was used to analyze the structure of rGO. Three points were measured for each powder to ensure the reliability of data.

**Wear Test**

Tribological properties of the coatings were examined using a reciprocating-type ball-on-disk tribometer (UMT-3, USA) under normal atmospheric conditions (temperature 27 °C, humidity 64%). Before the tribological tests, all samples were polished to the same roughness (about  $Ra = 0.1 \mu\text{m}$ ). The test was carried out under a load of 1 N

with an average sliding speed of 10 mm/s for 1200 s. The stroke length of the tests was 10 mm, and the total sliding distance was 12 m. The counterpart was a 316L stainless steel ball with a diameter of 3 mm. Before measurements, the balls were ultrasonically cleaned by ethanol, and a new ball was adopted for each test. The test for each sample was repeated three times. Wear loss in terms of wear volume was examined to evaluate the wear resistance of each sample using a three-dimensional surface profiler (Alpha-Step IQ, USA). The wear rate was calculated according to the following equation (Ref 11):  $W = V/(F \times L)$ , where  $W$ ,  $V$ ,  $F$  and  $L$  are the wear rate, the overall volume of the wear

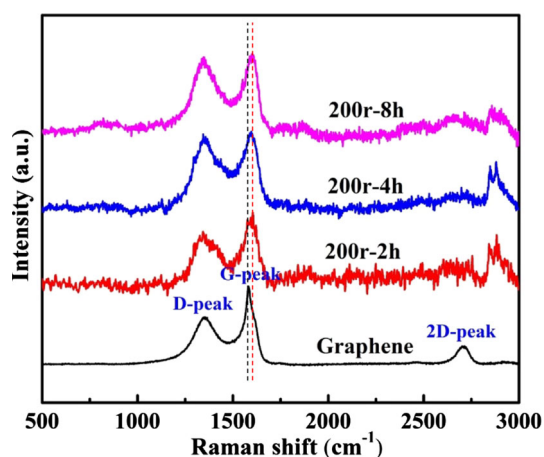


**Fig. 3** Raman spectra of the Al-0.1 wt.% rGO composite powder under different milling time

trace, the load and the sliding distance, respectively. Furthermore, the morphological features of the wear tracks were characterized using FESEM.

### Assessment of Electrochemical Properties

The potentiodynamic polarization curves of rGO-Al coatings were evaluated in 3.5 wt.% NaCl solution using a commercial electrochemical workstation (Modulab, 2100A, UK). A traditional three-electrode cell was employed, in which the working electrode was a coated substrate with an exposed area of 1 cm<sup>2</sup>, the reference electrode was a saturated calomel electrode to measure the potential across the electrochemical interface, and a platinum sheet (1 cm<sup>2</sup>) was used as the counter electrode. Before the electrochemical measurements, the coating samples were immersed in NaCl solution for 1 h. The electrochemical polarization was scanned at a velocity of 0.5 mV s<sup>-1</sup> over a potential range from - 500 to 500 mV. Corrosion potential and corrosion current density were measured via potentiodynamic polarization curves. Each test was repeated three times to ensure reproducibility.

## Results and Discussion

### Composite Powder

The microstructure of feedstock particles plays important roles in determining their deposition behaviors and the microstructure of resultant coatings. Accordingly, the evolution of the composite powder morphology as a function of the ball milling time was investigated (Fig. 2). The short ball milling time already triggered changes in the contour of the starting Al particles from near-spherical shape (Fig. 1a) to platelet (Fig. 2). Longer milling time

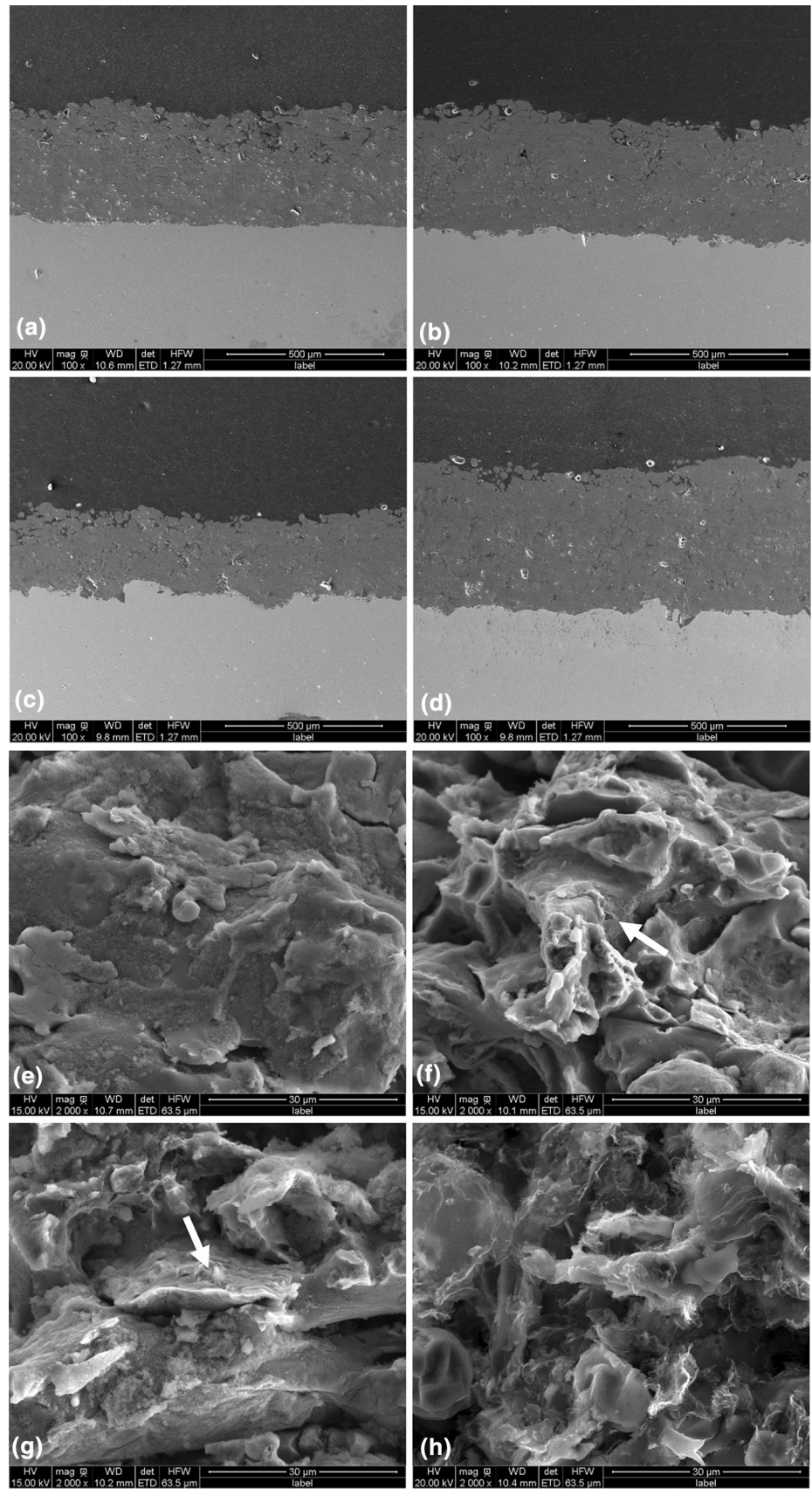
**Table 1** Raman data of Al-0.1 wt.% rGO particles under different milling time

State	$I_D/I_G$	$\omega_G$ , cm <sup>-1</sup>
Graphene	0.46 ± 0.13	1583 ± 1
200r-2 h	0.81 ± 0.06	1602 ± 8
200r-4 h	0.90 ± 0.06	1597 ± 3
200r-8 h	0.91 ± 0.05	1602 ± 2

gave rise to more flattened shape of the particles (Fig. 2a, b, and c). Enlarged views show disk-shaped Al particles (Fig. 2d, e, and f) and adherence of rGO sheets to the surfaces of the particles (as marked by the white arrow in Fig. 2g). EDS analyses further evidenced the presence of rGO sheets (Fig. 2i and k). It was reported that cold welding could be found for Al particles during milling (Ref 20, 25), which is also clearly recognized in this case (Fig. 2h). The cold welding phenomenon of Al particles reveals that rGO did not hinder the mechanical alloying process, and it is also believed that rGO can be rolled into the metallic matrix although the sheets cannot be distinguished due to their nanoscale dimensions. Besides the particle shape variation, different milling time also resulted in the variation of the particle size (Fig. 2j). The particle size of the composite powder increases with the increase in milling time (Ref 25).

The evolution of the structures of rGO sheets during milling was also characterized by Raman spectroscopy (Fig. 3). The Raman spectrum of the original rGO particles shows typical D-band, G-band, and 2D band peaks at 1349, 1573 and 2667 cm<sup>-1</sup>, respectively (Ref 10, 20, 26). The G-band refers to the plane breathing mode of sp<sup>2</sup> carbon atoms (Ref 6). The D-band is attributed to the defect and amorphous carbon of graphitic-based materials (Ref 15). The 2D-band is a main fingerprint of graphene. The shape, position and intensity of the 2D-band relative to the G-band usually reveal some important characteristics of rGO, such as defects, number of graphene layers. The intensity ratio of D-band to G-band ( $I_D/I_G$ ) usually reflects disorder and defect concentration of graphitic structures (Ref 10). It is noted that after milling for 2 h, the average  $I_D/I_G$  value of the rGO sheets increased from 0.46 to 0.81 (Table 1), suggesting the increase in disorder and defects in rGO sheets. Furthermore, the average  $I_D/I_G$  value continued to increase to 0.90 after milling for 4 h. As milling time was further elongated to 8 h, no marked change in  $I_D/I_G$  value was found, indicating that no further defect was introduced to the rGO sheet structure. This suggests that rGO nanosheets had already been embedded into Al particles, which can prevent further damage to the nanosheets (Ref 20). In addition, slight shifting of the G-band was

**Fig. 4** SEM images of cross-sectional microstructures of the pure Al (a), Al-0.1 wt.% rGO (b), Al-0.3 wt.% rGO (c) and Al-0.5 wt.% rGO (d) coatings and fracture morphologies of the pure Al (e), Al-0.1 wt.% rGO (f), Al-0.3 wt.% rGO (g) and Al-0.5 wt.% rGO (h) coatings



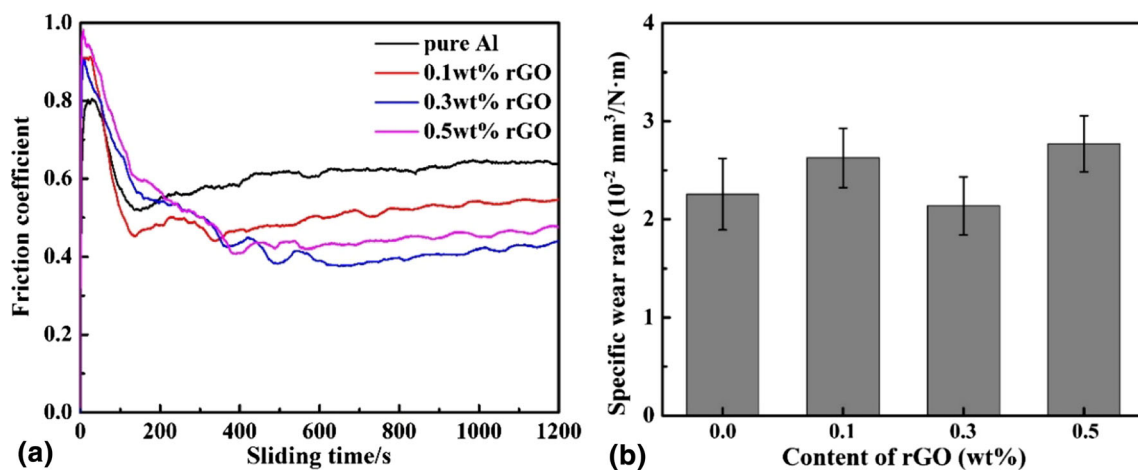


**Fig. 5** The friction coefficient (a) and wear rate (b) of the pure Al and composite coatings

recognized. The shift of the G-band ( $\omega_G$ ) might suggest residual stresses in rGO nanosheets due to the deformation of Al particles during milling. As shown in Table 1, the average wavenumber of G-band shifts from 1583 to 1602  $\text{cm}^{-1}$  after 2 h of milling. However, no marked increase in the average wavenumber could be seen with the milling time increasing to 4 and 8 h, indicating that the rGO would not experience significant deformation after milling for 2 h, which can also suggest that rGO nanosheets had already been embedded into Al particles after milling for 2 h.

### Microstructures and Properties of Coatings

The rGO-Al composite particles milled for 2 h were used as the original powder to fabricate composite coatings. The composite coatings with 0.1, 0.3 and 0.5 wt.% of rGO nanosheets were fabricated using flame spraying. The surface morphologies and cross-sectional microstructures of the composite coatings are shown in Fig. 4. It can be found that Al coatings and composite coatings present a dense microstructure (Fig. 4a, b, c and d). The addition of rGO into composite coatings did not alter their porosity. Figure 4(e), (f), (g), and (h) presents the fracture morphologies of the composite coatings. The rGO sheets marked by white arrows can be found on the surface of the fracture.

The tribological properties of the composite coatings including friction coefficient (COF) and wear rate were also investigated (Fig. 5). It can be found that COF experienced dramatic fluctuation during the initial run-in period, which is likely attributed to uneven contact between the mating surfaces (Fig. 5a). The curves present a steady state after 200 s as a dynamic equilibrium was achieved (Ref 15). It is clearly found that the COF of the composite coatings is much lower than that of the pure Al coating.

Moreover, the composite coatings containing 0.3 wt.% rGO showed the lowest COF among all the coatings, which can be attributed to the lubricating effect of rGO (Ref 14). It is also worth noting that COF of the composite coatings further increased when the content of rGO increased to 0.5 wt.%, which could be attributed to the aggregation of the rGO nanosheets due to the excessive addition (Ref 17). The specific wear rates of the coatings were also characterized and are shown in Fig. 5(b). Similar to the trend of the friction coefficient of the coatings, the addition of the 0.3 wt.% rGO sheets slightly reduced the average value of the specific wear rate of the coatings. Further characterization to the worn surfaces of the coatings was conducted using FESEM. The Al coatings show heavy plastic deformation (Fig. 6), suggesting the occurrence of adhesive wear. Different from the microcracks seen on the Al coatings, the microcracks can hardly be detected on the worn surface of the composite coatings.

Corrosion current density ( $I_{\text{corr}}$ ) and corrosion potential ( $E_{\text{corr}}$ ) were used to evaluate the corrosion resistance of samples (Ref 6, 11, 13, 17). The potentiodynamic polarization curves of the coatings are shown in Fig. 7 and Table 2. It is noted that  $I_{\text{corr}}$  of the pure Al coatings is slightly lower than that of the rGO-Al coatings, and  $E_{\text{corr}}$  of the pure Al coatings is higher than that of the rGO-Al coatings. Lower corrosion current density usually suggests the lower corrosion dynamic rate, and the higher corrosion potential may be related to a difficult tendency toward corrosion. In this case, it seems that the addition of rGO did not enhance the corrosion resistance of the Al coatings. For Al-based composite coatings, a protective oxide film usually enhances corrosion resistance, but the addition of reinforcing phase could lead to discontinuities in the film, which in turn increases the number of sites where corrosion could be initiated and renders the composite coatings liable to severe attack (Ref 6). The deteriorated anti-corrosion

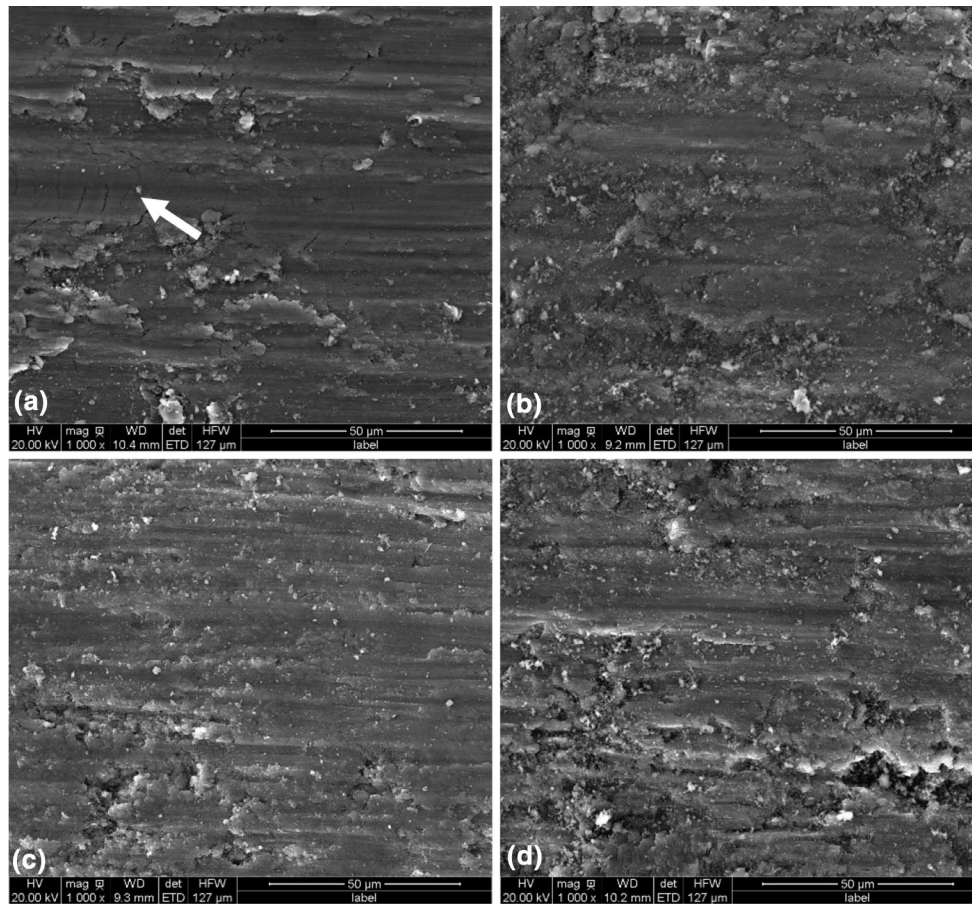


**Fig. 6** SEM images of wear tracks on the pure Al (a), Al-0.1 wt.% rGO (b), Al-0.3 wt.% rGO (c) and Al-0.5 wt.% rGO (d) coatings

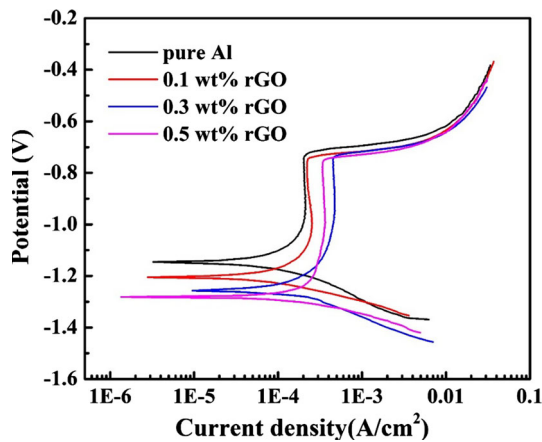


**Fig. 7** Potentiodynamic polarization curves of the pure Al and composite coatings

performances of the rGO-Al coatings might be related to the even presence of rGO nanosheets on the surfaces of the coatings. The exposed rGO consequently inhibits the continuous growth of aluminum oxide layer, giving rise to the worsened corrosion resistance in short-term incubation in the corrosive media. In addition, rGO nanosheets are

**Table 2** Electrochemical characteristics for pure Al and composite coatings in 3.5 wt.% NaCl solution

Samples	Corrosion current density ( $I_{corr}$ ), A/cm <sup>2</sup>	Corrosion potential ( $E_{corr}$ ) (V/SCE)
Pure Al	$5.33 \times 10^{-5}$	- 1.15
0.1 wt.% rGO	$5.93 \times 10^{-5}$	- 1.21
0.3 wt.% rGO	$1.03 \times 10^{-3}$	- 1.25
0.5 wt.% rGO	$1.46 \times 10^{-4}$	- 1.29

cathodic relative to the matrix, which could easily lead to galvanic corrosion in the presence of an electrolyte (Ref 16). The surface morphologies of the samples after electrochemical polarization testing were also characterized, and the result shows that some corrosion products can be found on the corroded surfaces, which presents the turtle crack structure (Fig. 8). The area of turtle cracks increases with the increase in the content of rGO in the coatings, suggesting more severe corrosion occurs due to the increase of the content of rGO in the coating.

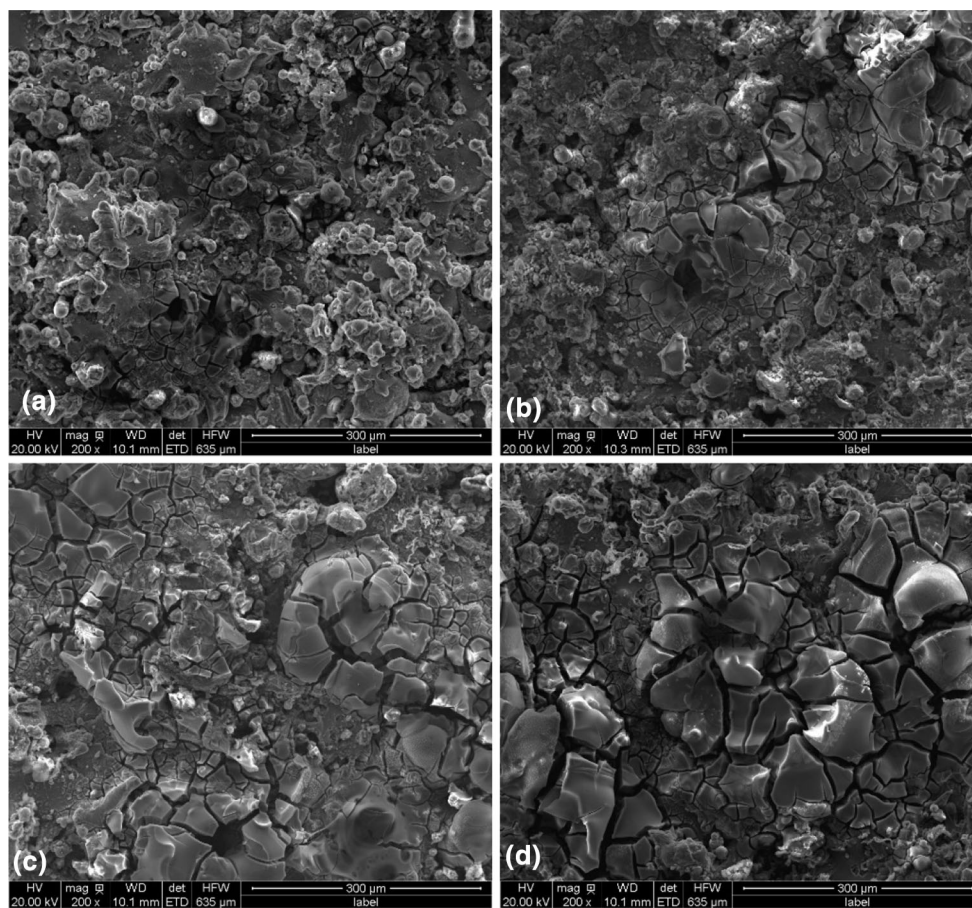


**Fig. 8** Surface morphologies of Al coatings (a), Al-0.1 wt.% rGO (b), Al-0.3 wt.% rGO (c) and Al-0.5 wt.% rGO (d) coatings after electrochemical tests

## Conclusions

Novel rGO-Al composites were fabricated by ball milling and flame spraying. The rGO nanosheets retained most their physicochemical features after ball milling with an increase in defects due to ball milling. The defects of rGO in the composite powder increased as the milling time increased in the early stage and then remained stable due to the embedment effect of Al particles. Unique dispersion of rGO in the coatings resulted in a low friction coefficient of the coatings. The addition of rGO nanosheets deteriorated the corrosion resistance of the composite coatings. Flame spraying together with ball milling would give a novel route to fabricate metal/graphene anti-friction materials.

**Acknowledgments** This work was supported by National Natural Science Foundation of China (21705158, 31500772), Key Research and Development Program of Zhejiang Province (2015C01036, 2107C01003), Fundamental Research Project of Qinghai Province (2016ZJ757), International Scientific and Technological Cooperation Project of Ningbo (2017D10011), Zhejiang Provincial Natural

Science Foundation of China (LY18C100003) and 3315 Program of Ningbo.

## References

1. K.S. Novoselov, A.K. Geim, S.V. Morozov, D. Jiang, Y. Zhang, S.V. Dubonos, I.V. Grigorieva, and A.A. Firsov, Electric Field Effect in Atomically Thin Carbon Films, *Science*, 2004, **306**(5696), p 666-669
2. T. Kuilla, S. Bhadra, D. Yao, N.H. Kim, S. Bose, and J.H. Lee, Recent Advances in Graphene Based Polymer Composites, *Prog. Polym. Sci.*, 2010, **35**(11), p 1350-1375
3. S.C. Tjong, Recent Progress in the Development and Properties of Novel Metal Matrix Nanocomposites Reinforced with Carbon Nanotubes and Graphene Nanosheets, *Mater. Sci. Eng. R*, 2013, **74**(10), p 281-350
4. S. Liu, L. Gu, H. Zhao, J. Chen, and H. Yu, Corrosion Resistance of Graphene-Reinforced Waterborne Epoxy Coatings, *J. Mater. Sci. Technol.*, 2016, **32**(5), p 425-431
5. S.J. Richard Prabakar, Y.H. Hwang, E.G. Bae, D.K. Lee, and M. Pyo, Graphene Oxide as a Corrosion Inhibitor for the Aluminum Current Collector in Lithium Ion Batteries, *Carbon*, 2013, **52**(2), p 128-136

6. M. Rashad, F. Pan, Z. Yu, M. Asif, H. Lin, and R. Pan, Investigation on Microstructural, Mechanical and Electrochemical Properties of Aluminum Composites Reinforced with Graphene Nanoplatelets, *Prog. Nat. Sci. Mater.*, 2015, **25**(5), p 460-470
7. L.A. Yolshina, R.V. Muradymov, I.V. Korsun, G.A. Yakovlev, and S.V. Smirnov, Novel Aluminum-Graphene and Aluminum-Graphite Metallic Composite Materials: Synthesis and Properties, *J. Alloys Compd.*, 2016, **663**, p 449-459
8. M. Rashad, F. Pan, A. Tang, and M. Asif, Effect of Graphene Nanoplatelets Addition on Mechanical Properties of Pure Aluminum Using a Semi-powder Method, *Prog. Nat. Sci. Mater.*, 2014, **24**(2), p 101-108
9. A. Bisht, M. Srivastava, R.M. Kumar, I. Lahiri, and D. Lahiri, Strengthening Mechanism in Graphene Nanoplatelets Reinforced Aluminum Composite Fabricated through Spark Plasma Sintering, *Mater. Sci. Eng. A*, 2017, **695**, p 20-28
10. Y. Cui, L. Wang, B. Li, G. Cao, and W. Fei, Effect of Ball Milling on the Defeat of Few-Layer Graphene and Properties of Copper Matrix Composites, *Acta Metall. Sin. Engl.*, 2014, **27**(5), p 937-943
11. M. Mo, W. Zhao, Z. Chen, Q. Yu, Z. Zeng, X. Wu, and Q. Xue, Excellent Tribological and Anti-corrosion Performance of Polyurethane Composite Coatings Reinforced with Functionalized Graphene and Graphene Oxide Nanosheets, *RSC Adv.*, 2015, **5**(70), p 56486-56497
12. C.H. Chang, T.C. Huang, C.W. Peng, T.C. Yeh, H.I. Lu, W.I. Hung, C.J. Weng, T.I. Yang, and J.M. Yeh, Novel Anticorrosion Coatings Prepared from Polyaniline/Graphene Composites, *Carbon*, 2012, **50**(14), p 5044-5051
13. J. Han, S. Ding, W. Zheng, W. Li, and H. Li, Microstructure and Anti-wear and Corrosion Performances of Novel UHMWPE/Graphene-Nanosheet Composite Coatings Deposited by Flame Spraying, *Polym. Adv. Technol.*, 2013, **24**(10), p 888-894
14. N. Li, L. Zhang, M. Xu, T. Xia, X. Ruan, S. Song, and H. Ma, Preparation and Mechanical Property of Electrodeposited Al-Graphene Composite Coating, *Mater. Des.*, 2016, **111**, p 522-527
15. R. Maurya, B. Kumar, S. Ariharan, J. Ramkumar, and K. Balani, Effect of Carbonaceous Reinforcements on the Mechanical and Tribological Properties of Friction Stir Processed Al6061 Alloy, *Mater. Des.*, 2016, **98**, p 155-166
16. F.H. Latief, E.S.M. Sherif, A.A. Almajid, and H. Junaedi, Fabrication of Exfoliated Graphite Nanoplatelets-Reinforced Aluminum Composites and Evaluating Their Mechanical Properties and Corrosion Behavior, *J. Anal. Appl. Pyrol.*, 2011, **92**(2), p 485-492
17. S. Ding, T. Xiang, C. Li, S. Zheng, J. Wang, M. Zhang, C. Dong, and W. Chan, Fabrication of Self-Cleaning Super-Hydrophobic Nickel/graphene Hybrid Film with Improved Corrosion Resistance on Mild Steel, *Mater. Des.*, 2017, **117**, p 280-288
18. D. Prasai, J.C. Tuberquia, R.R. Harl, G.K. Jennings, and K.I. Bolotin, Graphene: Corrosion-Inhibiting Coating, *ACS Nano*, 2012, **6**(2), p 1102-1108
19. F. Zhou, Z.T. Li, G.J. Shenoy, L. Li, and H.T. Liu, Enhanced Room-Temperature Corrosion of Copper in the Presence of Graphene, *ACS Nano*, 2013, **7**(8), p 6939-6947
20. M. Bastwros, G.Y. Kim, C. Zhu, K. Zhang, S. Wang, X. Tang, and X. Wang, Effect of Ball Milling on Graphene Reinforced Al6061 Composite Fabricated by Semi-solid Sintering, *Compos. Part B Eng.*, 2014, **60**(1), p 111-118
21. J. Huang, Y. Liu, J. Yuan, and H. Li, Al/Al<sub>2</sub>O<sub>3</sub> Composite Coating Deposited by Flame Spraying for Marine Applications: Alumina Skeleton Enhances Anti-corrosion and Wear Performances, *J. Therm. Spray Technol.*, 2014, **23**(4), p 676-683
22. W.S. Hummers and R.E. Offeman, Preparation of Graphitic Oxide, *J. Am. Chem. Soc.*, 1958, **80**(6), p 1339
23. M.J. McAllister, J.L. Li, D.H. Adamson, H.C. Schniepp, A.A. Abdala, J. Liu, M. Herrera-Alonso, D.L. Milius, R. Car, and R.K. Prud'homme, Single Sheet Functionalized Graphene by Oxidation and Thermal Expansion of Graphite, *Chem. Mater.*, 2007, **19**(18), p 4396-4404
24. Y. Liu, J. Huang, and H. Li, Synthesis of Hydroxyapatite-Reduced Graphite Oxide Nanocomposites for Biomedical Applications: Oriented Nucleation and Epitaxial Growth of Hydroxyapatite, *J. Mater. Chem. B*, 2013, **1**(13), p 1826-1834
25. S.S. Razavi-Tousi and J.A. Szpunar, Effect of Ball Size on Steady State of Aluminum Powder and Efficiency of Impacts during Milling, *Powder Technol.*, 2015, **284**, p 149-158
26. S.J. Yan, S.L. Dai, X.Y. Zhang, C. Yang, Q.H. Hong, J.Z. Chen, and Z.M. Lin, Investigating Aluminum Alloy Reinforced by Graphene Nanoflakes, *Mater. Sci. Eng. A*, 2014, **612**(33), p 440-444